Research Article

NMR IN BIOMEDICINE

Received: 29 September 2010, Revised: 04 March 2011, Accepted: 10 March 2011, Published online in Wiley Online Library: 2011

(wileyonlinelibrary.com) DOI: 10.1002/nbm.1724

Direct detection of a single evoked action potential with MRS in *Lumbricus terrestris*

Alexander J. Poplawsky[a], Raymond Dingledine[b] and Xiaoping P. Hu[c]*

Functional MRI (fMRI) measures neural activity indirectly by detecting the signal change associated with the hemodynamic response following brain activation. In order to alleviate the temporal and spatial specificity problems associated with fMRI, a number of attempts have been made to detect neural magnetic fields (NMFs) with MRI directly, but have thus far provided conflicting results. In this study, we used MR to detect axonal NMFs in the median giant fiber of the earthworm, *Lumbricus terrestris*, by examining the free induction decay (FID) with a sampling interval of 0.32 ms. The earthworm nerve cords were isolated from the vasculature and stimulated at the threshold of action potential generation. FIDs were acquired shortly after the stimulation, and simultaneous field potential recordings identified the presence or absence of single evoked action potentials. FIDs acquired when the stimulus did not evoke an action potential were summed as background. The phase of the background-subtracted FID exhibited a systematic change, with a peak phase difference of $(-1.2 \pm 0.3) \times 10^{-5}$ radians occurring at a time corresponding to the timing of the action potential. In addition, we calculated the possible changes in the FID magnitude and phase caused by a simulated action potential using a volume conductor model. The measured phase difference matched the theoretical prediction well in both amplitude and temporal characteristics. This study provides the first evidence for the direct detection of a magnetic field from an evoked action potential using MR. Copyright © 2011 John Wiley & Sons, Ltd.

Keywords: action potential; magnetic resonance spectroscopy; neural magnetic field; earthworm

INTRODUCTION

Functional MRI (fMRI) is a widely used technique for the investigation of *in vivo* neural activation by indirect measurement of the signal changes that arise from the hemodynamic response as a result of increased metabolic demand. This hemodynamic response lacks spatial specificity as it is localized to the vasculature near the neural activity, rather than the neural activity itself, and does not possess sufficient temporal resolution to provide the timing of the neuronal event. The direct measurement of neural magnetic fields (NMFs) with MR can, in principle, provide a more spatially and temporally accurate measurement of brain function, and has been the goal of a number of recent efforts.

Investigators initially detected transient magnetic fields using MRI in water phantoms that conducted currents at physiological magnitudes (1–3). Computational modeling predicted the MRI signal change caused by NMFs to be much smaller than the signal change attributed to the hemodynamic response (4–7). *In vivo* studies in human subjects provided contradictory results on the detection of NMFs (8–16). One probable reason was that the change associated with *in vivo* neural activity could not be separated completely from the hemodynamic response. *In vitro* studies that physically decoupled the neural tissue from the vascular system successfully detected NMFs that appeared to be associated with increased neural activity (17–19), with the exception of a recent study in isolated turtle brain (20). However, no study has examined the effect of an evoked NMF using an MR method with a temporal resolution that is sufficient to capture the evolution of an action potential. The aim of this study is to provide definitive experimental evidence for the direct detection of an evoked NMF using fast temporal resolution MRS.

We chose the median giant fiber (MGF) system of the earthworm, *Lumbricus terrestris*, for the following reasons. First, the removal of the nerve cord from the vascular system is possible. Second, the two major giant axons contained in the ventral nerve cord have been well described in terms of their anatomy and electrophysiology. The lateral giant fibers (LGFs) are two electrically coupled axons that function as a single unit. The MGF is a single, larger diameter axon that is located between the two lateral fibers (Fig. 1), and was the focus of the current study. Both fiber systems are physiologically involved in the rapid shortening reflex of the earthworm body (21), and the activity of axon and muscle potential changes can be identified using extracellular recordings (22). Third, it is possible to evoke a single action potential from the MGF that is uncomplicated by any other event. This includes activity of the LGF, which has a higher threshold of activation, and therefore can

* *Correspondence to: X. P. Hu, Emory University – Hospital Annex, 531 Asbury Circle, Suite N307, Atlanta, GA 30322–4600, USA.*
E-mail: xhu@bme.emory.edu

a *A. J. Poplawsky*
Neuroscience Program, Emory University, Atlanta, GA, USA

b *R. Dingledine*
Department of Pharmacology, Emory University, Atlanta, GA, USA

c *X. P. Hu*
Department of Biomedical Engineering, Emory University, Atlanta, GA, USA

Abbreviations used: *AP, action potential; FID, free induction decay; fMRI, functional MRI; I_e, extracellular current; I_i, intracellular current; LEI, Lorentz effect imaging; LGF, lateral giant fiber; MGF, median giant fiber; nAP, no action potential; NMF, neural magnetic field.*

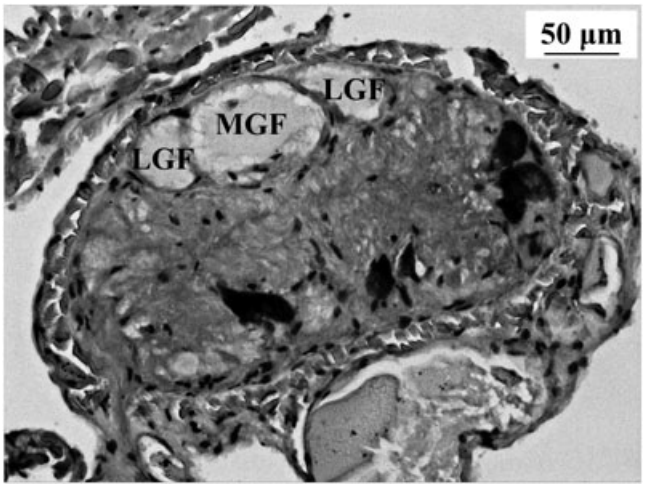

Figure 1. Section through the isolated earthworm nerve cord. The median giant fiber (MGF) separates the two electrically coupled lateral giant fibers (LGF); 9-µm paraffin section stained with hematoxylin.

remain quiescent during MGF action potential generation. Finally, action potentials can be elicited from the isolated nerve cord at room temperature and the preparation does not require oxygen gas perfusion. The latter attribute reduces concerns with regard to paramagnetic oxygen affecting the MR signal (23).

A previous study employed a volume conductor model and predicted the magnetic field generated by a single evoked action potential from the measured intracellular potential (24). Furthermore, Roth and Wikswo (25) experimentally verified this model by measuring the magnetic field directly using a toroid pickup coil. They measured a Δ300-pT magnetic field from the giant axon system of the crayfish, which is physiologically similar to the earthworm giant axon system. Likewise, a Δ300-pT magnetic field was within the range detected in water phantoms (1,2), and provides confidence that the earthworm action potential will be above the detection threshold for our methods.

Simultaneous field potential recordings and MRS were performed to measure the voltage and magnetic field associated with a single evoked action potential. Spectroscopy was used in a manner similar to that employed by Ernst and Hennig (26) such that the free induction decay (FID) was examined in the time domain providing a submillisecond temporal resolution. In a previous study, Petridou *et al*. (19) analyzed the frequency domain of the FID in spontaneously active organotypic rat brain cultures. They showed a phase difference, and a lesser magnitude difference, at the frequencies of electroencephalographic recordings obtained outside of the MRI. In contrast, the present study measured the FIDs following evoked nerve cord stimulation in a time-locked fashion and examined the differences in the time domain signal between the presence and absence of an action potential. In addition to this experiment, a volume conductor model was adapted to calculate the FID magnitude and phase change from a previously reported intracellular recording of an earthworm action potential (27). The MRS experiment showed a phase change that was in agreement with the theoretical predictions of the volume conductor model.

EXPERIMENTAL DETAILS

Earthworm nerve cord preparation

Earthworms (*Lumbricus terrestris*; Kennesaw Bait Co., Marietta, GA, USA) were anesthetized in 10% ethanol for 5 min, or until the escape reflex was abolished, and submerged in a 0 °C dissection chamber containing worm saline (77.0 mM Na^+, 4.0 mM K^+, 6.0 mM Ca^{2+}, 1.0 mM Mg^{2+}, 43.0 mM Cl^-, 26.0 mM SO_4^{2-}, 2.0 mM Tris, 55.0 mM sucrose, 167.0 mOsm and pH 7.4) (28). A longitudinal incision was made along the dorsal midline to access the ventral nerve cord. The nerve cord was then isolated from the worm by gently peeling the cord from the ventral epithelial wall and cutting any connective tissue. The worm saline was changed every 15 min for the duration of the dissection. Once the nerve cord had been removed, it was transferred to 4 °C saline and allowed to acclimate to room temperature before being transferred to the chamber for simultaneous field potential recordings and MRS.

Chamber allowing simultaneous field potential recordings and MRS

The chamber used to record simultaneous field potentials and MRS was constructed with two compartments linked by a glass capillary bridge (inner diameter, 0.7 mm; outer diameter, 1 mm) and was filled with worm saline (Fig. 2). The first compartment contained a pair of bipolar AgCl hook stimulating electrodes (separation, 1 mm) and the entrance AgCl hook recording electrode (located directly before the entrance of the capillary bridge). The second compartment contained the exit AgCl hook recording electrode (located directly after the exit of the capillary bridge) and the common reference AgCl electrode. A custom radiofrequency transmit and receive microcoil (inner diameter, 1 mm; number of turns, 7; copper wire diameter, 0.405 mm; coil length, 4 mm; enamel insulation thickness, 20 µm) was wound

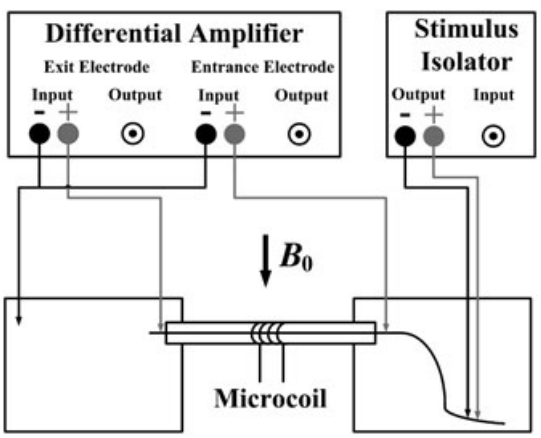

Figure 2. Chamber allowing simultaneous field potential recordings and MRS. The anterior nerve cord was stimulated with bipolar electrodes at the threshold of action potential generation. This resulted in interleaved events with and without action potentials. Evoked action potentials were first recorded by the entrance electrode and followed by the exit electrode. The difference in arrival time of the action potential between the two electrodes was used to calculate the conduction velocity. The conduction velocity was then used to determine the time at which the action potential arrived at the custom radiofrequency microcoil.

NMR IN BIOMEDICINE

tightly around the glass capillary bridge and fixed with cyanoacrylate. The radiofrequency microcoil recorded the FID.

The anterior end of the nerve cord was pinned over both stimulating electrodes and gently drawn through the capillary bridge and through the center of the radiofrequency microcoil by applying slight suction. The nerve cord fitted tightly within the inner walls of the capillary bridge and was turned until the MGF was located at the bottom edge of the capillary's inner diameter. In this way, the MGF was positioned asymmetrically at the bottom extreme of the microcoil's sensitive volume, as the MGF is located on the dorsal surface of the nerve cord (Fig. 1). The posterior end of the cord was secured over the exit electrode and the remaining nerve cord was gently stretched and secured over the entrance electrode. All fastening pins were nonmagnetic cactus spikes.

Data acquisition – electrophysiology

Action potentials were recorded with a Digidata 1320A (Axon Instruments, Sunnyvale, CA, USA) in response to nerve cord stimulation by a pulse generator (Master-8, A.M.P.I., Jerusalem, Israel). A stimulus pulse with a delay of 1.0 ms and width of 0.3 ms was used. The amplitude of the pulse was controlled by a stimulus isolator (A360 stimulus isolator, World Precision Instruments, Sarasota, FL, USA). The threshold stimulation for action potential generation was determined before each trial by adjusting the stimulus magnitude to elicit action potentials about half the time. The stimulus amplitude was maintained constant within a single trial, but was reset to the action potential threshold between trials, if necessary. The two recording and one reference electrode measured the extracellular field potential differentially (Differential AC Amplifier, Model 1700, A-M Systems, Sequim, WA, USA). The following parameters were used: repetitions per trial, 500; sampling bandwidth, 10 kHz; sampling duration, 2.05 s; inter-stimulus interval, 4 s; low pass filter, 1 kHz; high pass filter, 300 Hz. Clampex 9.2 (Axon Instruments) stored the amplified, filtered and digitized electrophysiological time courses.

Data acquisition – MRS

The chamber was placed at the isocenter of a 9.4-T Bruker Biospin (Billerica, MA, USA) with the nerve cord arranged perpendicular to the static magnetic field. The following parameters were used: FID sampling bandwidth, 3.125 kHz; flip angle, 90°; TR = 2.0 s; repetitions per trial, 1000; dummy scans, 6. Each experiment lasted 7–10 h. The transmit and receive microcoil used quadrature detection to simultaneously acquire the real and imaginary components of the FID. During even TRs, the MRS protocol was initiated without triggering nerve cord stimulation. This group was used in post-processing steps to correct for phase drift. During odd TRs, the nerve cord was stimulated at the threshold of action potential generation. Two interleaved subgroups resulted during the odd TRs because of the all-or-nothing nature of the action potential – action potential (AP) and no action potential (nAP) subgroups.

A radiofrequency excitation delay was determined at the start of each trial according to the trial-specific conduction velocity calculated by linear extrapolation of the difference in arrival times of the action potential at the two recording electrodes. This delay was calculated in order to fix the arrival of the action potential at 0.5 ms after the start of FID acquisition (Fig. 3). No magnetic field gradients were used during the experiment.

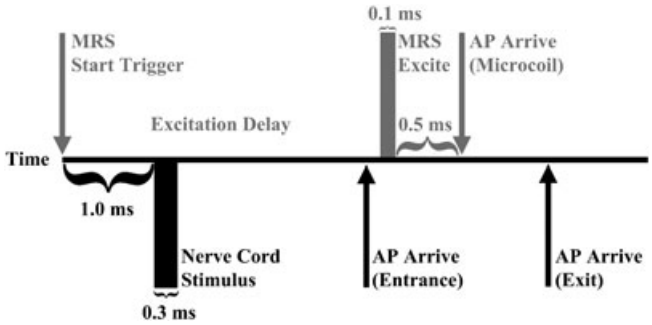

Figure 3. Timing diagram of the simultaneous field potential recordings (black text) and MRS (gray text) experiment. A trigger from the MRS protocol initiated the field recording digitizer and the nerve cord stimulus pulse generator (delay, 1.0 ms; width, 0.3 ms). A trial-specific excitation delay was calculated according to the predetermined conduction velocity of the action potential (AP) between the entrance and exit field recording electrodes. The MRS excitation (width, 0.1 ms) was timed so that the action potential arrived at the radiofrequency microcoil 0.5 ms after the start of free induction decay (FID) acquisition.

Within a single experiment, if action potentials could no longer be elicited from the nerve cord, further trials were discontinued. If the nerve cord was healthy for at least seven full trials (with a maximum of 12 trials), the worm was considered for further data analysis.

Data analysis – electrophysiology

Field potentials were acquired from both recording electrodes for every TR. Using Clampfit 9.2 (Axon Instruments), each repetition was separated into the components that corresponded to the even and odd TRs, respectively. The absences of stimulation artifact and nerve cord activity were verified in the even TR group and were not used for further analysis. The presence or absence of an action potential event was then identified for each odd TR trace using a Clampfit 9.2 threshold detection program, and separated into AP and nAP subgroups, respectively. Finally, the baseline for each trace was corrected to zero.

Data analysis – MRS

The interleaved MRS time courses were separated into odd and even TR groups. The phase information was processed by multiplying individual odd TR FIDs by the complex conjugate of the subsequent even TR FID. The MRS time courses were then separated into AP and nAP subgroups according to the electrophysiological recordings that were acquired simultaneously. The phase of the FID was calculated and filtered (eight-pole Bessel bandpass filter, Clampfit 9.2, Axon Instruments) to remove frequencies outside of the 240–437.5-Hz range. This range included physiological frequencies of the action potential and minimized filtering artifacts.

Correction of action potential timing based on the conduction velocity

A single action potential reference trace was chosen for each worm, and individual action potential electrophysiology traces were shifted in time around it. A 'shift value' was accepted when a maximum positive Pearson's linear correlation coefficient was achieved between the two traces. The shift value is the amount

of time an individual action potential trace required to achieve maximal alignment with the reference trace. This correction was performed only on exit electrode time courses, and the shift values were then used to shift the corresponding FID and entrance electrode time courses. Events that showed a correlation coefficient three standard deviations below that of the mean correlation coefficient of a single worm were rejected from further analysis. Once the action potentials had been temporally aligned, the mean action potential minimum was used to normalize the electrophysiological data.

The nAP subgroup FIDs were also shifted to control for the effects of the action potential alignment process. This was performed by assigning shift values to individual nAP FIDs that were randomly sampled from the accepted AP subgroup shift values. Shift values from the AP and nAP subgroups were then compared using a *t*-test to verify that they were from the same population with at least 95% confidence. The process of shifting the nAP FIDs was repeated 100 times and averaged to ensure reproducibility of the nAP waveform presented in Fig. 4B.

Modeled MR magnitude and phase change

The theoretical model of Woosley *et al*. (24) was used to calculate the magnetic field of the earthworm MGF using a previously reported earthworm intracellular potential recording (27).

$$B(\rho,k) = \mathrm{i}\mu_0 akI_1(|k|a)K_1(|k|\rho)\left\{\frac{\sigma_\mathrm{i}}{\beta(|k|a)} - \frac{\sigma_\mathrm{e}}{\alpha(|k|a)}\right\}\varphi_\mathrm{m}(k) \quad [1]$$

where ρ is the radial distance from the axon center, k is the spatial frequency, B is the spatial Fourier transform of the magnetic field at distance ρ, μ_0 is the permeability of free space, a is the axon radius, I_1 and K_1 are modified Bessel functions, α and β are defined by the Bessel functions, σ_i and σ_e are the intracellular and extracellular conductivities, respectively, and $\varphi_\mathrm{m}(k)$ is the spatial Fourier transform of the intracellular potential (24). The simulated volume had the same radius as the capillary bridge (0.35 mm) and same length as the solenoid microcoil (4.00 mm). In a cross-section of the simulated volume, the simulated MGF occupied the bottommost position of the plane and B_0 horizontally crossed MGF in order to match the experimental conditions. The component of the generated magnetic field parallel to B_0 was calculated at varying distances within the simulated volume. The following values were used to calculate the magnetic field of a single action potential: $\rho = 36$–4000 µm, $a = 35$ µm, $u = 14.7$ m/s, $\sigma_\mathrm{i} = 1.70$ S/m and $\sigma_\mathrm{e} = 2.06$ S/m.

The magnitude and phase changes associated with the calculated axonal magnetic field were determined:

$$\varphi(r,\theta,l,t) = \gamma\int B(r,\theta,l,t)\mathrm{d}t \quad [2]$$

$$M\mathrm{e}^{\mathrm{i}\Delta\varphi(t)} = \frac{M_0}{V}\iiint r\cdot\mathrm{e}^{\mathrm{i}\varphi(r,\theta,l,t)}\mathrm{d}r\ \mathrm{d}\theta\ \mathrm{d}l \quad [3]$$

The resultant phase (φ) was determined for each time point (t) of the calculated magnetic field over the sensitive volume of the solenoid radiofrequency microcoil (V), where r is the glass capillary inner diameter, θ is the radial angle, l is the length of the microcoil and γ is the proton gyromagnetic ratio. Finally, the MR magnitude (M) and phase change ($\Delta\varphi$) were calculated in time, where M_0 is the equilibrium magnetization.

Kao and Grundfest's (27) description of the spike rise time, peak potential amplitude and time of spike decay to baseline were considered in reconstructing the intracellular recording and used in our theoretical simulation. The MGF radius was measured experimentally. Isolated nerve cords were fixed in 4% paraformaldehyde for 60 min, cut into coronal sections and embedded in paraffin. Blocks were cut at 9 µm, deparaffinized and stained with hematoxylin (GTX73341, GeneTex, Inc., Irvine, CA, USA). The radius of the MGF in the posterior nerve cord was calculated from its circumference using an Axio Scope Observer.A1 and AxioVision 4.7 (Carl Zeiss MicroImaging GmbH, Jena, Germany).

A Pearson's linear correlation was performed between the theoretical and experimental phase time courses. In order for a point-by-point analysis to be performed, several adjustments

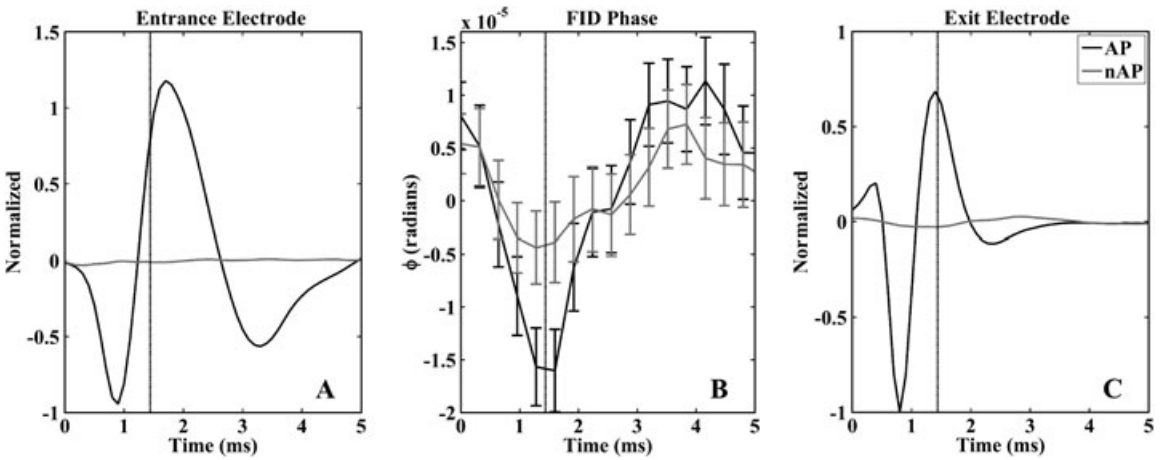

Figure 4. Averaged time course of the action potential field at the entrance (A) and exit (C) of the capillary bridge and the averaged free induction decay (FID) phase (B). Averaged time courses with the presence of an action potential (AP subgroup) are marked with a solid black line, whereas those identified as not having an action potential (nAP subgroup) are marked with a solid gray line. The action potential arrived at the radiofrequency microcoil 0.5 ms after the start of FID acquisition. The action potential conduction velocity was used to adjust the electrophysiological time courses in (A) and (C) to be consistent with the arrival of the action potential at the microcoil in (B) in order to synchronize all traces. In this way, the vertical lines represent the same relative cycle of the action potential that corresponds to the trough of the FID phase. Error bars represent the standard error of the mean and the numbers (n) of AP and nAP time courses are 16 718 and 12 920, respectively.

were made. The sampling interval of the theoretical simulation was adjusted to that of the experimental interval (0.32 ms). The theoretical phase minimum value was preserved during this process and the phase change was set to begin at approximately 0.5 ms. The latter adjustment synchronized the arrival of the theoretical action potential with the experimental action potential, which was calculated to arrive 0.5 ms after the start of FID acquisition.

RESULTS

Measuring an evoked action potential with simultaneous electrophysiology and MRS

The nerve cords of six earthworms (59 trials) with a weight of 4.90 ± 0.05 g (mean ± standard error of the mean) before dissection and an average conduction velocity (u) at room temperature of 14.7 ± 0.1 m/s were used. A total of 29 638 electrophysiological traces was obtained, with 16 718 (56%) having an action potential (AP subgroup) and 12 920 (44%) exhibiting no action potential (nAP subgroup).

The field recordings measured activity from the entire nerve cord at the location of the electrode. The stimulus intensity was adjusted to evoke a single action potential at the entrance and exit electrodes (Fig. 4A and 4C, respectively). The absence of other extracellular potentials verified the successful isolation of the MGF action potential from all other cellular components. The temporal evolution of the action potential was consistent throughout the course of each experiment, suggesting that the preparation was stable over the course of a 7–10-h experiment.

No change could be identified in either the magnitude or phase of a single FID trace. However, the mean AP and nAP FID traces of all six worms (Fig. 4B) revealed a difference in phase, but not in magnitude, that was associated in time with the action potential. The peak trough had a group-averaged difference in phase (AP – nAP) of $(-1.1 \pm 0.3) \times 10^{-5}$ radians at 1.28 ms and $(-1.2 \pm 0.3) \times 10^{-5}$ radians at 1.60 ms, respectively.

Theoretical modeling of the MR magnitude and phase change

Two isolated nerve cords, from earthworms weighing 4.55 and 5.09 g before dissection, were used to measure the MGF radius. The MGF radius of the posterior nerve cord was 35.1 ± 0.8 µm, calculated from the circumference of 45 nerve cord sections. Simulation of an earthworm action potential indicated a maximum magnitude change of -2.39×10^{-9}% (Fig. 5A) and phase change of -0.69×10^{-5} radians (Fig. 5B) in the FID. The predicted magnitude change was below the detection threshold for our MRS method by at least four orders of magnitude. The measured and simulated phase changes, however, were of similar magnitude. The magnitude and phase returned to baseline at the completion of the action potential.

Correlation of theoretical and experimental results

A Pearson's linear correlation between the simulated and experimental phase changes had a correlation coefficient (r_e) of 0.802 ($p < 0.001$, $n = 17$ time points for each trace) (Fig. 6).

DISCUSSION

Our results demonstrate the feasibility of detecting an evoked axonal action potential in the absence of the hemodynamic response. MRS detected a significant phase change, but not a magnitude change, in the FID that corresponded in time with simultaneous electrophysiological recordings of the action potential. The amplitude of the FID-averaged phase change was similar to the theoretical phase change determined using a volume conductor model. These experiments provide definitive evidence for the direct detection of an NMF by MRS that agrees with the theoretical prediction in both temporal profile and amplitude.

Technical considerations

There were small variations in conduction velocity within a single trial that resulted in action potentials arriving at the entrance and exit electrodes at slightly different times. The misalignment

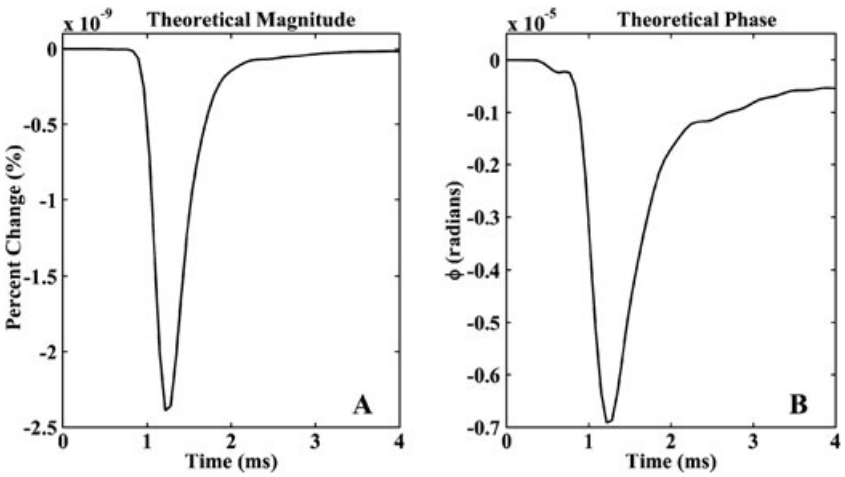

Figure 5. The median giant fiber (MGF) transmembrane potential of a single evoked action potential was described by Kao and Grundfest (27) and used in our theoretical simulation. The theoretical MR magnitude (A) and phase (B) time courses were calculated for a single earthworm action potential. The following parameters were used to calculate the theoretical time courses: $\rho = 36$–4000 µm, $a = 35$ µm, $u = 14.7$ m/s, $\sigma_i = 1.70$ S/m and $\sigma_e = 2.06$ S/m.

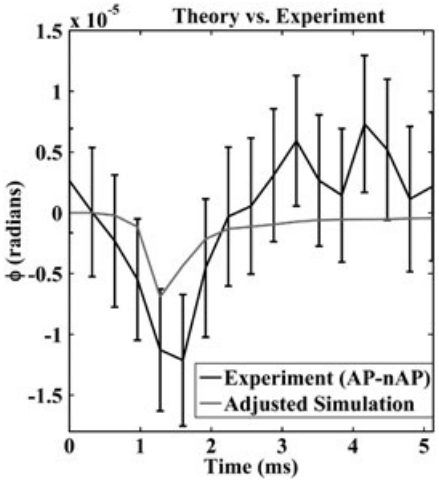

Figure 6. The average subtracted free induction decay (FID) phase (AP – nAP, solid black line) correlated well with the simulated phase change (solid gray line) [correlation coefficient (r_e) = 0.802, $p < 0.001$, $n = 17$ time points for each trace]. The error bars represent the 95% confidence intervals for the subtraction. The adjusted simulation has the same sampling bandwidth and action potential arrival time as the experiment. AP, action potential; nAP, no action potential.

of action potentials resulted in a blurred group-averaged field potential. This action potential misalignment would also have occurred at the microcoil and would cause a temporal blurring of the average FID. Electrophysiological data from the exit electrode were used to correct for this misalignment by registering each action potential to a reference trace. The single electrode registration was then used to correct for the timing misalignment at the entrance electrode as well as the FID signal. This correction assumed that the conduction velocity was constant between the entrance and exit electrodes. Although there is some evidence of variation in the conduction velocity along the length of the earthworm nerve cord (29,30), action potentials having a fast conduction velocity (1.4 cm/ms) allow for an acceptable approximation over the short distances between the entrance and exit electrode (2.7 cm) and the microcoil center and exit electrode (1.4 cm).

A slow variation was seen in the nAP subgroup average (Fig. 4B). This was most probably a result of the current injection applied to stimulate the nerve cord. This effect was controlled for in the present study by keeping the experimental conditions identical for AP and nAP subgroups and examining the difference (Fig. 6).

We reported a theoretical (Fig. 5B) and an adjusted (Fig. 6) phase simulation. The adjusted simulation included adjustments based on the sampling interval and the action potential arrival time of the experiment. It was possible to compare the simulation directly with the experimental results following these adjustments. The time course of the adjusted simulation was correlated significantly with the experimental phase changes in both temporal characteristics and peak minima. Yet, the experimental phase peak appeared wider in time than the simulation. This difference might be attributed to less accurate correction of the action potential misalignment as the distance increased from the exit electrode.

The effect of the MGF radius on the depth of the theoretical phase minimum was also examined. It is known that the processes of fixing and embedding cause tissue shrinkage (31,32). Although the degree of shrinkage for this specific tissue is not known, the radius of the MGF was reported to be between 34 and 47 μm, with the radius decreasing from anterior to posterior (29). An approximately linear relationship between the predicted phase minimum and the MGF radius was observed across this range. For every 2 μm increase in the radius, the phase minimum deepened by -0.09×10^{-5} radians.

Lastly, we did not consider the magnetic field that existed inside the MGF in the theoretical modeling. Previous studies did not validate this component of the magnetic field with experimental results and it was omitted to achieve a more conservative model. The magnetic field inside the MGF would cause only a slightly larger simulated FID phase change as the omitted volume accounts for only 1% of the total volume seen by the microcoil.

Volume conductor model

Roth and Wikswo compared an experimentally recorded axon magnetic field (25) with one that was predicted by the volume conductor model (24). Their measured magnetic field showed significant consistency with the predicted field in both magnitude and temporal evolution. In addition, the toroid detector from which Roth and Wikswo recorded the axon magnetic field was similar to the radiofrequency microcoil detector in our experiment. Both types of detector average the magnetic field over the circumference and length of the detector. For these reasons, we were confident that an adaptation of the volume conductor model would correctly predict the MR magnitude and phase change following an evoked action potential using our methods.

The volume conductor model predicts the total axon magnetic field from the individual contributions of the extracellular and intracellular currents, I_e and I_i, respectively. It has been determined previously that the magnetic field caused by I_e is orders of magnitude less than the magnetic field caused by I_i (24). In this way, a good approximation of the total axon magnetic field can be calculated by considering only the contribution of I_i. The intracellular current conducting longitudinally through a defined axonal compartment can be characterized as an equivalent current dipole (Q_i) and is a relevant measure of brain activity that is often used in the discussion of magnetoencephalographic and electroencephalographic measurements. The equivalent current dipole is a vector quantity described by the equation $Q_i = I_i L d\boldsymbol{r}$ (7,33), where L is the MGF length within the microcoil (4 mm) and $d\boldsymbol{r}$ is a unit direction vector. The volume conductor model was extended to estimate I_i from the same MGF intracellular potential as implemented previously to approximate the FID phase and magnitude changes (27). I_i was estimated to have a maximum change of −247.7 nA in time, which corresponds to an equivalent current dipole of −1.0 nA m within the length of the microcoil.

Symmetrical *vs* asymmetrical distribution of the NMF

Chow *et al.* (15) examined the phase changes that resulted from a symmetrically and asymmetrically distributed NMF within a volume of interest. They determined that the magnetic field must be asymmetrically distributed in the volume for a phase change to be detected, as a net zero phase change resulted from a symmetrically distributed magnetic field. A solenoid microcoil with an asymmetrically positioned axon was used in

our experiment and theoretical simulation. The earthworm nerve cord was tightly contained within the inner walls of the capillary bridge and the MGF was located at the bottom edge of the capillary's inner diameter in our experiment. From this position, an adaptation of the volume conductor model predicted the component of the MGF magnetic field that was parallel to B_0. In this way, the MGF bipolar magnetic field was asymmetrically distributed in the volume of interest and resulted in a detectable phase change.

A circular surface microcoil positioned above the capillary bridge and perpendicular to the MGF is an alternative method of investigating the phase change associated with the axon NMF. A coil of this design has diminishing sensitivity to the proton signal as the distance from the surface coil increases, and permits an asymmetric sensitivity to the phase change caused by the axon NMF. In this way, a surface microcoil design may enhance the detectability of the phase change, as it is more sensitive to a single pole of the NMF, in contrast with our solenoid design which is equally sensitive to both poles.

Physiology of the phase change

The shape of the FID phase difference in both the predicted and measured time courses is caused by the opposing sodium and potassium currents that occur during an action potential. The action potential begins with the depolarizing stimulus at the anterior end of the MGF. Depolarization opens fast-acting voltage-gated sodium channels and allows an inward flux of sodium ions into the axon. This inward current creates a magnetic field that temporarily opposes the external magnetic field, resulting in a decrease in the net magnetic field and a drop in the FID phase. The voltage-gated sodium channels quickly inactivate and prevent the flux of new sodium ions from entering the axon. At a similar time as the sodium channels inactivate, slower activating voltage-gated potassium channels open and allow potassium ions to leave the axon. This opposing outward current reverses the magnetic field generated by the axon and subsequently increases the net magnetic field and returns the FID phase to baseline. This temporal evolution on a submillisecond scale requires an MR method that has sufficient temporal resolution, as demonstrated by our experiment.

The simulated phase change in Fig. 6 shows two points at times 3.20 and 4.16 ms to be outside of the experimental phase change confidence intervals. These time points are above zero radians, suggesting that the refocusing magnetic field generated by the axon is stronger than the theoretically predicted magnetic field. A stronger refocusing magnetic field may be caused by a greater outward potassium current that corresponds to a hyperpolarization of the axon in the final stages of the action potential. The intracellular recording of Kao and Grundfest (27), used in our theoretical simulation, did not have an axon hyperpolarization component and this may be a result of differences in the physiological saline solutions of the two experiments. The extracellular saline solution of our experiment was consistent with the ionic composition measured in the coelomic fluid of the earthworm (28), whereas that of Kao and Grundfest (27) was not. This difference could result in a change in the inward and outward current characteristics of each experiment. However, the intracellular recording of Kao and Grundfest (27) is an appropriate approximation because the phase change associated with the hyperpolarizing component of the action potential will contribute very little to the total magnetic field change. This is evident in our observations, as other simulated phase points between 2.88 and 5.12 ms are within the 95% confidence intervals of the experimental phase change.

Lorentz effect imaging (LEI)

LEI and its application to the direct detection of magnetic fields have been shown in current-carrying phantoms (34,35) and *in vivo* (36). The Lorentz force is the spatial displacement of a current-carrying conductor in the presence of an external magnetic field that is equal to the cross-product of the current vector and the magnetic field. MR contrast arises from the Lorentz force by the spatially incoherent displacement of water protons caused by the conductor's compression of the surrounding elastic medium or by the bulk movement of water by ionic current flux (37). LEI is sensitive to this displacement with the use of time-locked oscillating magnetic field gradients that cause a loss of phase coherence and a decrease in the MR signal magnitude. The Lorentz effect occurs at a time simultaneous to the electrical activity and can confound our study.

In our case, the axon displacement caused by the Lorentz force should not lead to a significant change in signal phase because of the absence of time-locked gradients and the acquisition of the NMR signal from the rigid capillary. Applied magnetic field gradients, including spatial encoding gradients, were absent in our experiment. In addition, the close correlation of the simulated and observed FID phase changes provides further evidence that Lorentz forces may contribute a phase change that is significantly less than the change associated with the axon NMF. However, a displacement of the axon towards the center of the capillary may reduce the asymmetry in our set-up and produce a more symmetrical magnetic field in the volume of interest, resulting in a reduction in the observed phase change. Based on the experimental data of Truong *et al.* (35), and assuming the worst case scenario where the cord movement is not restricted by the rigid capillary, our estimated axon displacement is 5 μm and the estimated reduction in the depth of the phase minimum is $+0.01 \times 10^{-5}$ radians. This number is much less than the observed and simulated peak depths of -1.2×10^{-5} and -0.69×10^{-5} radians, respectively.

Extrapolation to *in vivo* studies and application

Previous studies have measured a magnitude, but not a phase, change in the MRI signal following visual stimulation of the human optic nerve at 1.5 T (14,15). However, a similar study failed to replicate these findings at 3 T and attributed this failure to increased magnetic susceptibility artifacts at the higher field (16). We have demonstrated through experiment and simulation that the phase of the MR signal is more sensitive to evoked axonal magnetic fields and that the effect of the axonal magnetic fields on the MR signal takes place on a millisecond timescale. The latter aspect would call for MR studies with a high temporal resolution, as demonstrated here. For *in vivo* studies on this subject, spectroscopic imaging with the examination of time domain data may be used.

The volume conductor model is also able to predict the intracellular membrane potential from the measured magnetic field (24,25). In combination with our method for the detection of NMFs, *in vivo* axon function can be measured following activation. Such a noninvasive study of neural currents localized to specific nerve fiber bundles could be developed further to

establish the characteristics of action potential propagation in normal and disease states, such as multiple sclerosis. However, confounders attributable to the hemodynamic response to nerve activation, which was absent in our experiment, would need to be addressed for application to *in vivo* studies.

CONCLUSIONS

Direct detection of a single evoked axonal magnetic field in the earthworm was demonstrated using simultaneous MRS and electrophysiology in the absence of the hemodynamic response. This experiment was validated by comparing the measured FID phase change with an adaptation of the volume conductor model of Woosley *et al*. (24). We also showed that the phase of the FID returned to baseline at the cessation of the axonal event and that a method with a high temporal resolution is required to resolve such transient NMFs, therefore validating MRS as an alternative method for the direct detection of neural activity.

Acknowledgements

This research was partly funded by the Emory University PRISM Fellowship and the GK-12 program of the National Science Foundation (NSF), Award #DGE0536941, National Institutes of Health (NIH) grant RO1EB002009, the Georgia Research Alliance and NIH grant 5U01 NS058158-05.

REFERENCES

1 Bodurka J, Bandettini PA. Toward direct mapping of neuronal activity: MRI detection of ultraweak, transient magnetic field changes. Magn. Reson. Med. 2002; 47: 1052–1058.
2 Konn D, Gowland P, Bowtell R. MRI detection of weak magnetic fields due to an extended current dipole in a conducting sphere: a model for direct detection of neuronal currents in the brain. Magn. Reson. Med. 2003; 50: 40–49.
3 Pell GS, Abbott DF, Fleming SW, Prichard JW, Jackson GD. Further steps toward direct magnetic resonance (MR) imaging detection of neural action currents: optimization of MR sensitivity to transient and weak currents in a conductor. Magn. Reson. Med. 2006; 55: 1038–1046.
4 Xue Y, Gao J-H, Xiong J. Direct MRI detection of neuronal magnetic fields in the brain: theoretical modeling. Neuroimage, 2006; 31: 550–559.
5 Park TS, Lee SY. Effects of neuronal magnetic fields on MRI: numerical analysis with axon and dendrite models. Neuroimage, 2007; 35: 531–538.
6 Blagoev KB, Mihaila B, Travis BJ, Alexandrov LB, Bishop AR, Ranken D, Posse S, Gasparovic C, Mayer A, Aine CJ, Ulbert I, Morita M, Muller W, Connor J, Halgren E. Modelling the magnetic signature of neuronal tissue. Neuroimage, 2007; 37: 137–148.
7 Cassarà AM, Hagberg GE, Bianciardi M, Migliore M, Maraviglia B. Realistic simulations of neuronal activity: a contribution to the debate on direct detection of neuronal currents by MRI. Neuroimage 2008; 39: 87–106.
8 Xiong J, Fox PT, Gao J-H. Directly mapping magnetic field effects of neuronal activity by magnetic resonance imaging. Hum. Brain Mapp. 2003; 20: 41–49.
9 Bianciardi M, Di Russo F, Aprile T, Maraviglia B, Hagberg GE. Combination of BOLD-fMRI and VEP recordings for spin-echo MRI detection of primary magnetic effects caused by neuronal currents. Magn. Reson. Imaging, 2004; 22: 1429–1440.
10 Liston AD, Salek-Haddadi A, Kiebel SJ, Hamandi K, Turner R, Lemieux L. The MR detection of neuronal depolarization during 3-Hz spike-and-wave complexes in generalized epilepsy. Magn. Reson. Imaging, 2004; 22: 1441–1444.
11 Chu R, de Zwart JA, van Gelderen P, Fukunaga M, Kellman P, Holroyd T, Duyn JH. Hunting for neuronal currents: absence of rapid MRI signal changes during visual-evoked response. Neuroimage, 2004; 23: 1059–1067.
12 Konn D, Leach S, Gowland P, Bowtell R. Initial attempts at directly detecting alpha wave activity in the brain using MRI. Magn. Reson. Med. 2004; 22: 1413–1427.
13 Parkes LM, de Lange FP, Fries P, Toni I, Norris DG. Inability to directly detect magnetic field changes associated with neuronal activity. Magn. Reson. Med. 2007; 57: 411–416.
14 Chow LS, Cook GG, Whitby E, Paley MNJ. Investigating direct detection of axon firing in the adult human optic nerve using MRI. Neuroimage, 2006; 30: 835–846.
15 Chow LS, Cook GG, Whitby E, Paley MNJ. Investigation of MR signal modulation due to magnetic fields from neuronal currents in the adult human optic nerve and visual cortex. Magn. Reson. Imaging, 2006; 24: 681–691.
16 Chow LS, Dagens A, Fu Y, Cook GG, Paley MN. Comparison of BOLD and direct-MR neuronal detection (DND) in the human visual cortex at 3T. Magn. Reson. Med. 2008; 60: 1147–1154.
17 Park TS, Lee SY, Park J-H, Lee SY. Effect of nerve cell currents on MRI images in snail ganglia. Neuroreport, 2004; 15: 2783–2786.
18 Park TS, Lee SY, Park J-H, Cho MH, Lee SY. Observation of the fast response of a magnetic resonance signal to neuronal activity: a snail ganglia study. Physiol. Meas. 2006; 27: 181–190.
19 Petridou N, Plenz D, Silva AC, Loew M, Bodurka J, Bandettini PA. Direct magnetic resonance detection of neuronal electrical activity. Proc. Natl. Acad. Sci. USA 2006; 103: 16 015–16 020.
20 Luo Q, Lu H, Lu H, Senseman D, Worsley K, Yang Y, Gao J-H. Physiologically evoked neuronal current MRI in a bloodless turtle brain: detectable or not? Neuroimage, 2009; 47: 1268–1276.
21 Rushton WAH. Reflex conduction in the giant fibres of the earthworm. Proc. R. Soc. London, Ser. B. 1946; 133: 109–120.
22 Drewes CD. *Escape Reflexes in Earthworms and Other Annelids*. Plenum Press: New York, NY, 1984.
23 Luo Q, Liu H-L, Parris B, Lu H, Senseman DM, Gao J-H. Modeling oxygen effects in tissue-preparation neuronal-current MRI. Magn. Reson. Med. 2007; 58: 407–412.
24 Woosley JK, Roth BJ, Wikswo JP. The magnetic field of a single axon: a volume conductor model. Math. Biosci. 1985; 76: 1–36.
25 Roth BJ, Wikswo JP. The magnetic field of a single axon. A comparison of theory and experiment. Biophys. J. 1985; 48: 93–109.
26 Ernst T, Hennig J. Observation of a fast response in functional MR. Magn. Reson. Med. 1994; 32: 146–149.
27 Kao CY, Grundfest H. Postsynaptic electrogenesis in septate giant axons. I. Earthworm median giant axon. J. Neurophysiol. 1957; 20: 553–573.
28 Drewes CD, Pax RA. Neuromuscular physiology of the longitudinal muscle of the earthworm, *Lumbricus terrestris*. I. Effects of different physiological salines. J. Exp. Biol. 1974; 60: 445–452.
29 McFall JL, Landa KB, Drewes CD. Parameters of giant fiber conduction in intact, freely moving earthworms. Am. Zool. 1977; 17: 876.
30 O'Gara B, Vining EP, Drewes CD. Electrophysiological correlates of rapid escape reflexes in intact earthworms, *Eisenia foetida*. I. Functional development of giant nerve fibers during embryonic and postembryonic periods. J. Neurobiol. 1982; 13: 337–353.
31 Ross KFA. Cell shrinkage caused by fixatives and paraffin-wax embedding in ordinary cytological preparations. Q. J. Microsc. Sci. 1953; 94: 125–139.
32 Hillman H. Limitations of clinical and biological histology. Med. Hypotheses, 2000; 54: 553–564.
33 Murakami S, Okada Y. Contributions of principal neocortical neurons to magnetoencephalography and electroencephalography signals. J. Physiol. 2006; 575: 925–936.
34 Song AW, Takahashi AM. Lorentz effect imaging. Magn. Reson. Imaging, 2001; 19: 763–767.
35 Truong T-K, Wilbur JL, Song AW. Synchronized detection of minute electrical currents with MRI using Lorentz effect imaging. J. Magn. Reson. 2006; 179: 85–91.
36 Truong T-K, Song AW. Finding neuroelectric activity under magnetic-field oscillations (NAMO) with magnetic resonance imaging in vivo. Proc. Natl. Acad. Sci. USA, 2006; 103: 12 598–12 601.
37 Truong T-K, Avram A, Song AW. Lorentz effect imaging of ionic currents in solution. J. Magn. Reson. 2008; 191: 93–99.